International J. Geomagnetism and Aeronomy, v.5, issue 1.

Observations of neutral winds and electric fields using backscatter from field-aligned irregularities

L.M. Kagan[12], S. Fukao and M. Yamamoto

Research Institute for Sustainable Humanosphere, Kyoto University, Japan

P.B. Rao

National Remote Sensing Agency, Department of Space, Balanagar, Hyderabad 500 037, AP, India

Abstract. We propose an experiment, a data-processing procedure, and a method to recover the electric fields and neutral winds, which are the driving forces for field-aligned irregularity (FAI) generation, from the range-time distribution of line-of-sight Doppler velocities during type-2 backscatter events in the ionospheric E region. In doing so we proceed from the fact that ionospheric parameters, specifically the collisional frequencies, change noticeably over the radar height resolution. The proposed technique is based on our knowledge of the mechanisms for FAI generation, the models of the ionospheric parameters and the morphology of the observed velocities. We illustrate our method with a case study for the MU radar on the night of July 25, 2002. The method proposed does not require any additional funding and may be used at sites where the coherent scatter radar has a height resolution which is one half of the minimum desired resolution of the energy sources: neutral winds and electric fields.

1. Introduction

Neutral winds and electric fields dominate the dynamics in the E region where backscatter from the E-region field-aligned irregularities is observed. In general, ionospheric parameter measuring techniques can be divided into two groups: remote and direct. Electric fields are measured *in situ* by instruments which are mounted on rockets, balloons or satellites using a double-probe technique (*Kelley,* 1989; *Schunk and Nagy,* 2000).

Neutral winds are measured both *in situ* and remotely. In the case of direct observations, a chemical release is used as a tracer for measuring neutral winds in the mesosphere and lower thermosphere. The chemical release technique provides wind data for the altitude range covering the entire E region with a high altitude resolution of about 100 m or so. A detailed review of the winds measured by the chemical release technique over more than 40 years may be found in *Larsen* (2002).

Remote diagnostics of ionospheric winds are mainly based on Doppler measurements and have been accomplished with different types of radar: meteor, mesosphere-stratosphere-troposphere (MST) and MF and optical interferometers (see for example, *Jacka,* 1984; *Roper,* 1984; *Rottger*, 1984; *Hocking,* 1997; *Hocking et al.,* 2001 and references therein). Neutral winds were also measured by the wind imaging interferometer on board NASA's Upper Atmosphere Research Satellite (*Shepherd et al*., 1993).

All these techniques are characterized by their cost, availability at the location of interest, time and altitude resolution and altitudes covered. *In situ* observations require special efforts and funding. They are expensive and relatively rare. Nevertheless, several experimental campaigns expressly aimed at

[1]On extended leave from Radiophysical Research Institute, Nizhniy Novgorod, Russia.

[2] Now at University of Western Ontario, London ON, Canada

studying ionospheric processes in the E region (sporadic-E layers, in particular) and involving rocket measurements of winds and electric fields were carried out. Among those recently organized are the SEEK-I (see *Larsen et al.,* 1998; *Pfaff et al.,* 1998; *Fukao et al.,* 1998 and references therein) and SEEK-II campaigns in Japan.

The remote techniques for measuring winds suffer from a limitation on the altitude range (they work mainly below 100 km altitude). Also the altitude resolution isn't as good as that of the chemical release technique. For meteor radars the altitude and time resolutions depend on the number of meteors; for example, in the case study presented below, they were about 2 km and 2 hours, respectively.

It should be mentioned that for cases in which backscatter from field-aligned irregularities is observed from altitudes either well below or well above 100 km, the measured Doppler velocities may be attributed correspondingly to either a neutral wind or electric field alone (*Kagan,* 2002). Based on this *Murthy et al.* (1998) extracted meridional winds from the backscatter data below 97 km altitude measured by the Gadanki radar in India. *Patra* (2002) applied the same idea to deriving zonal winds at 90-97 km from the backscatter observed by *Tsunoda and Ecklund* (1999) at Pohnpei.

In this paper we propose an experimental method and a data-processing procedure which allow the altitude-time reconstruction of background and polarization electric fields and neutral winds in the backscatter regions from the altitude-time distribution of line-of-sight Doppler velocities observed with a coherent scatter radar (CSR). This method doesn't require any additional expense. The altitude and time resolution of our method are equal to twice the altitude resolution and equal to the temporal resolution of the radar measurements, respectively.

To this end we have to solve two basic problems. First, we have to reconsider the theories of 3-m irregularity generation (most coherent-scatter radars observe at frequencies close to 50 MHz; for example, the MU radar frequency is 46.5 MHz) to find a more correct expression for the phase velocity which takes into account neutral gas motions and ion magnetization (Section 2). Second, we have to develop an experimental scheme and a data-processing procedure to extract the desired information from observations by making use of the above theory (Section 3). We show the efficiency and limits of our method using the middle and upper (MU) radar as a basic instrument in Section 4. We discuss the validity and further development of the method in Section 5.

2. Secondary gradient drift waves in the ionospheric E region.

Traditionally, electric fields have been assumed as a source for both the Farley-Buneman [*Farley*, 1963; *Buneman*, 1963; *Sudan,* 1983] and gradient drift [*Rogister and D'Angelo,* 1970; *Sudan et al,* 1973; *Fejer and Kelley*, 1980; *etc.*] instabilities. For a long time neutral winds had been assumed to have magnitudes of about 50 m/s or less. This might have been in part because there has been no theory either predicting or explaining winds as strong as 100 m/s or higher, although sounding rockets have measured neutral winds using a chemical release as a tracer since 1958. The majority of these observations weren't widely published, but instead presented either in internal institution reports or conference proceedings. The measurements of wind velocities of about 150 m/s near 106 km altitude during the SEEK campaign [*Larsen et al.,* 1998], and the publication of the theory of the neutral wind-driven gradient drift instability [*Kagan and Kelley,* 1998] immediately following these measurements,

turned minds towards the role of neutral motions in E-region small-scale structuring.

Recently *Larsen* [2002] reviewed all sources of wind measurements over 40 years and showed that the neutral wind velocity exceeded 100 m/s in more than 60% of observations and that the wind maximum was located between 100 and 110 km altitude. Such winds may be a source of free energy themselves for gradient drift [*Kagan and Kelley*, 1998; *Kagan,* 2002] and for thermal processes [*Kagan and Kelley*, 2000; *Kagan et al.,* 2000; *Dimant and Oppenheim,* 2003].

The true driving force for these instabilities is a polarization electric field appearing as a result of local charge separation (electron and ion) [*Kagan*, 2002]. This polarization field may be much stronger than the background electric field and at midlatitudes may map along the geomagnetic field line for large distances [*Cosgrove and Tsunoda,* 2001; *Yokoyama et al,* 2003; 2004].

[*Sudan et al.*, 1973] showed that 3-m gradient-drift irregularities observed with 50-MHz radars can't be induced directly and were the result of secondary gradient drift processes. In the *Sudan et al.* [1973] scenario the gradients, necessary for the secondary gradient drift instability (GDI) to develop, were provided by primary gradient drift waves. These primary waves, larger-scale inhomogeneities with the wave length λ_{pr}, produced the polarization electric field, which played the role of an external electric field for secondary plasma perturbations with wave length $\lambda_{sec} << \lambda_{pr}$.

McDonald et al. (1975) studied numerically the generation of secondary small-scale gradient-drift irregularities and found that irregularities with $\lambda_{sec} < 28$ m are excited only after the amplitude of the larger-scale primary waves reached 4% of the background plasma density. This result is consistent with the theory of small-scale irregularity generation due to secondary gradient drift processes.

Although there are fewer rocket measurements of midlatitude small-scale irregularities than in the equatorial E region, this two-step process seems to be the case for midlatitudes as well. Thus, for example, *Bowhill* (1966) and *Itoh et al.* (1975) detected small-scale plasma irregularities associated with midlatitude sporadic E with rocket-borne Langmuir probes. *Bowhill's* (1966) estimates gave a vertical scale of these irregularities of about 25 m and a broadband amplitude of the irregularities of about 5-10%; *Itoh et al.* (1975) reported the broadband amplitude of 4-100 m waves to be about 1-5% of the background density; *Kelley et al.* (1995) observed a burst of waves with an estimated wavelength of 1-100 m near 110 km altitude and they reported the presence of few-kilometer-scale waves throughout the entire flight. The amplitude of the 60-600 m primary waves was about 7% of the background density.

In their theory, *Sudan et al.* (1973) assumed that the background electric fields were the only instability source. Cooperation of neutral winds and electric fields for primary wave generation is discussed in [*Kagan,* 2002].

The development of the theory of secondary gradient drift waves presented herein follows the lines of the linear theory developed for the primary waves by *Kagan and Kelley* [1998] and similar to that suggested by *Sudan et al.* [1973] for electric field-driven processes.

Under routine operation most coherent scatter radars observe backscatter in the meridional plane perpendicular to the geomagnetic field lines and at frequencies close to 50 MHz. Thus, the detected signal is backscattered by irregularities with a typical scale close to 3 m. The meter-scale irregularities can't be generated directly and are the result of secondary gradient drift processes in which the primary waves serve a double purpose for

these secondary waves: they act as the regular gradient and they create a polarization electric field playing the role of the external electric field. For this routine geometry of the experiment the radar measures backscatter from meter-scale (secondary) irregularities with the wave vector along the radar line-of-sight in the meridional plane. Thus, the primary waves for these meter-scale irregularities should have the wave vector perpendicular to both the wave vector of the secondary waves ($k_y^{\sec}$ below) and the geomagnetic field, i.e. in the zonal direction. These primary waves can be considered as a regular plasma gradient for secondary gradient drift waves if

$$k_y^{\sec} \cdot \lambda_x^{pr} >> 1, \qquad (2.1)$$

where $k_y^{\sec}$ is the radar line-of-sight wave vector of the secondary wave and λ_x^{pr} is the zonal wavelength of the primary wave [*Sudan et al.,* 1973]. Here we have chosen a Cartesian coordinate system relative to the routine operation of most radars (the MU radar in particular) (Fig. 1), *i.e.*, the $\hat{z}$ axis is along the geomagnetic field $\mathbf{B_0}$, the $\hat{x}$ axis is eastward, and the $\hat{y}$ axis is aligned with the radar line-of-sight (southward and downward).

The dimensionless plasma density $n=N/N_0$ (N is the plasma density and N_0 is the background plasma density) for the secondary processes may be written as

$$n = 1 + n_{pr} + n_1, \qquad (2.2)$$

where n_{pr} is the dimensionless plasma density fluctuation in the primary wave and n_1 is the dimensionless plasma density.

The primary irregularities embedded in the background plasma create a background for the secondary processes. The meridional Doppler velocity observed by the radar is the phase velocity of the secondary gradient drift waves and is due to electron drift in the crossed electric and geomagnetic fields and ion motion driven by neutral wind. The expression for the line-of-sight phase velocity of the secondary wave (in the following, if not stated otherwise, by 'line-of-sight velocity' we mean the line-of-sight velocity routinely observed by CSRs, i.e. in the meridional plane) is similar to that for the primary wave,

$$V_{ph,\sec,y} = \frac{V_{e,\sec,y} + \psi \cdot V_{i,\sec,y}}{(1+\psi)}. \qquad (2.3)$$

Here $V_{e,sec,y}$ is the electron drift velocity in the crossed total imposed electric ($\mathbf{E_{0x}}$+$\mathbf{E_{pol,x}}$ below) and geomagnetic $\mathbf{B_0}$ fields; $V_{i,\sec}$ represents ion drag by moving neutrals; and

$$\psi = \psi_0 \left[\frac{\omega_e^2 k_z^2}{\nu_{en}^2 k^2} + \frac{k_\perp^2}{k^2} \right], \quad \psi_0 = \frac{\nu_{en}\nu_{in}}{\omega_e \omega_i} \qquad (2.4)$$

where ν_{en}, ν_{in} and ω_e, ω_i are the collisional and gyro frequencies of the electrons and the ions. In (2.4) and below we omit the subscript "sec" for the wave vector of the secondary waves.

The polarization electric field $\mathbf{E_{pol,x}}$, originated in the primary processes, may be quite strong and together with the background electric field $\mathbf{E_{0x}}$ acts as an external electric field for the secondary gradient drift waves. The line-of-sight electron and ion velocities of the secondary waves in Eq. (2.3), respectively, are:

$$V_{e,\sec,y} = \frac{E_{0x} + E_{\mathrm{pol},x}}{B_0} \qquad (2.5)$$

Figure 1

$$V_{i,\sec,y} = \frac{u_{ny} - q_i u_{nx}}{1+q_i^2} + \frac{q_i E_{0y} - q_i^2 E_{0x}}{1+q_i^2}, \qquad (2.6)$$

where $\mathbf{u_n}$ is the neutral wind velocity.

The polarization electric field may be written as [*Kagan and Kelley,* 2000]:

$$\mathbf{E_{pol}} = -\frac{\mathbf{u_0}}{D}\frac{k_T T}{e} n_{pr}, \qquad (2.7)$$

where

$D = (D_{iz} + D_{ez}) \cdot \cos^2 \alpha + (D_{i\perp} + D_{e\perp}) \cdot \sin^2 \alpha$ is the diffusion coefficient; D_{iz}, $D_{i\perp}$ and D_{ez}, $D_{e\perp}$ are the field-aligned and field-perpendicular diffusion coefficients of ions and electrons, respectively; α is the angle between **k** and $\mathbf{B_0}$; k_T is the Boltzmann constant; T is the temperature, which at the altitudes of interest may be considered the same for electrons, ions and neutrals; e is the magnitude of the elementary charge; $\mathbf{u_0} = \mathbf{V_{i0}} - \mathbf{V}_{e0}$ is the background current velocity, i.e. the relative velocity between electrons and ions; and $\mathbf{V_{i0}}$ and $\mathbf{V_{e0}}$ are the zero-order ion and electron velocities, respectively.

The aspect sensitivity angle, which is the complementary angle to α, is measured to be less than 1°. For E-region altitudes this gives $D \cong [k_T T / M\nu_{in}](1+\psi)$.

The zonal component of the polarization electric field (2.7) contributing to the meridional electron velocity (2.5) is

$$E_{pol,x} = -u_{0x} B_0 \frac{n_{pr}}{q_i(1+\psi)}, \qquad (2.8)$$

where the zonal zero-order current velocity is

$$u_{0x} = -\frac{E_{0y} - q_i E_{0x}}{B_0(1+q_i^2)} + \frac{u_{nx} + q_i u_{ny}}{(1+q_i^2)}, \qquad (2.9)$$

and

$$q_i = \frac{\omega_i}{\nu_{in}}. \qquad (2.10)$$

Note that for the lower E region (isotropic ions, q_i<<1) the zonal current velocity is defined by the electron drift in the crossed meridional electric and geomagnetic fields and by the ion drag by a zonal neutral wind.

Eqs. (2.8-2.10) lead to

$$E_{pol,x} = \frac{\left(q_i^{-1} E_{0y} - E_{0x} - \left[q_i^{-1} u_{nx} + u_{ny}\right] B_0\right) n_{pr}}{\left[(1+q_i^2)(1+\psi)\right]} \qquad (2.11)$$

Eq. (2.3), taking into account (2.5), (2.6) and (2.11), gives the following phase velocity along the radar line-of-sight for the secondary gradient waves

$$V_{ph,\sec,y} = (1+\psi)^{-1} \left\{ \frac{E_{0x}}{B_0} + \frac{u_{0x} n_{pr}}{q_i(1+\psi)} + \psi \frac{u_{ny} - q_i u_{nx}}{(1+q_i^2)} \right\} \qquad (2.12)$$

In Eq. (2.12) we have neglected the term $\psi (q_i E_{0y} - q_i^2 E_{0x}) / (1+q_i^2)$ compared to E_{0x}.

Note that for the lower E-region case (q_i<<1), and for zero neutral winds, (2.12) gives the expression for the phase velocity of secondary waves derived by *Sudan et al.* [1973].

There is a very important notion related to the observational use of the above formulas, Eqs. (2.3) and (2.12). Coherent radars observe the line-of-sight Doppler velocity, which is the phase velocity of irregularities backscattering the radar signal. Independently of the nonlinearity of the processes producing the small-scale irregularities, this line-of-sight phase velocity, to leading order, is the same as for linear processes. Moreover, it is the same for the different instabilities: gradient-drift, thermal and Farley-Buneman. However, for the latter process one should keep in mind that, although the phase velocity is described by the same formula, observations have shown that Farley-Buneman waves always move at their threshold speed, which is close to the ion acoustic speed c_s (due to the ψ factor adjustments).

In more sophisticated experimental procedures when CSR observes backscatter signal from small-scale irregularities perpendicularly to the geomagnetic field line but the radar beam doesn't lie in the meridional plane, the line-of-sight phase velocity is

$$V_{ph,\mathrm{sec}} = V_{ph,\mathrm{sec},y}\sin\beta + V_{ph,\mathrm{sec},x}\cos\beta\,, \qquad (2.13)$$

where β is the angle between the radar line-of-sight and zonal directions; $V_{ph,\mathrm{sec},y}$ is defined by (2.12) and $V_{ph,\mathrm{sec},x}$ is:

$$V_{ph,\mathrm{sec},x} = (1+\psi)^{-1}\left\{\frac{E_{0y}}{B_0} - \frac{u_{0y}n_{pr}}{q_i(1+\psi)} + \psi\frac{u_{nx}+q_i u_{ny}}{(1+q_i^2)}\right\} \qquad (2.14)$$

and

$$u_{0y} = \frac{E_{0x}+q_iE_{0y}}{B_0(1+q_i^2)} + \frac{u_{ny}-q_iu_{nx}}{(1+q_i^2)}\,. \qquad (2.15)$$

The growth rate of the secondary GDI is

$$\gamma_{\mathrm{sec}} = \frac{\psi}{(1+\psi)\nu_{in}}\left[\frac{\mathbf{k}\cdot\mathbf{u}_{0,\mathrm{sec}}}{(1+\psi)^2} - c_s^2k^2\right] + \frac{\mathbf{k}\cdot\mathbf{u}_{0,\mathrm{sec}}\nu_{in}k_{\mathrm{los}}}{(1+\psi)^2\omega_i\lambda_{pr}k^2} \qquad (2.16)$$

where k_{los} is the radar line-of-sight wave vector of the secondary waves. For the routine observational geometry $k_{\mathrm{los}} = k_y$.

The first term in brackets describes the two-stream processes. For the gradient drift instability the velocities are much less than the ion acoustic speed and the two-stream term may be neglected. For the routine radar geometry at the condition of marginal stability

$$\frac{u_{0,\mathrm{sec},y}}{\lambda_{pr}} = c_s^2k^2q_i(1+\psi)\frac{\psi}{\nu_{in}}\,. \qquad (2.17)$$

The right-hand part of (2.17) is defined by the ionospheric parameters ψ, ν_{in}, ω_i, and c_s, which are functions of altitude,

location and time. These parameters may be found using the models. Neither of the values on the left-hand side of (2.17) is known. However, to satisfy our initial assumption $k_y^{\sec} \cdot \lambda^{pr} >> 1$ and based on observations (*Kelley et al.*, 1995) one may suppose λ^{pr} to be of the order of 100 m for 3-m irregularities observed by the 46.5-MHz MU radar ($\lambda^{\sec} \cong 3.2$ m).

It should be mentioned that the primary waves, which provide a regular plasma density gradient, are not necessarily caused by gradient drift processes. The only requirement is that these primary waves should have a wave vector perpendicular to the geomagnetic direction and appear due to the same source as the secondary waves. Thus, the role of primary waves may be played by the irregularities excited by thermal processes (*Kagan and Kelley*, 2000; *Dimant and Sudan,* 1997; *Dimant and Oppenheim,* 2003), for example. The wave vector of these thermal irregularities is perpendicular to B_0, thus providing the equatorial-like geometry for secondary GDI generation. The wave vector of the primary waves is perpendicular to both the wave vector of the secondary waves and to the geomagnetic field. Thus, for the secondary waves observed in the meridional plane, the primary waves should have a wave vector in the zonal direction.

Note that the scenario considered doesn't discuss the energy transfer from long wavelengths to short ones. For stationary turbulence the energy input at long wavelengths is balanced by energy dissipation at short wavelengths. To find the power spectrum of stationary turbulence, one may follow the scheme proposed by *Sudan* (1983) for the equatorial electrojet, with appropriate corrections from neutral wind inputs into the linear GDI growth rate (see *Kagan and Kelley,* 1998). The effects of turbulence on the width of signal spectra received by radars operated in the frequency range between 2 MHz and several hundred megahertz are reviewed in *Hocking* (1985).

3. Method for observing electric fields and neutral winds with backscatter from field-aligned irregularities (FAI).

Most coherent scatter radars (CSRs) are operated at a frequency close to 50 MHz and observe perpendicularly to the geomagnetic field in the meridional plane. The backscatter signal is very aspect sensitive and disappears when the radar beam deviates by about ±0.5° from perpendicularity. Since 3-m irregularities can't be generated directly, the line-of-sight Doppler velocity observed in the meridional plane is the line-of-sight phase velocity of the secondary waves. The beauty is that, independently of complexity and nonlinearity of the processes resulting in 3-m irregularities, their phase velocity is described to leading order by the same expression (Eq. (2.12)).

3.1. Identities of the contributors to the phase velocity in the E region.

The obvious problem which one will face here is that from the measurements of only one parameter, namely the line-of-sight Doppler velocity, we are going to find several unknown ionospheric parameters: zonal and meridional electric fields and neutral winds. So, to succeed we obviously need some additional information and assumptions.

Below we demonstrate the basis of the method for the routine observational geometry when the radar observes in the meridional plane. Assuming that the line-of-sight Doppler velocity is the phase velocity of the secondary gradient-drift

waves, the phase velocity of secondary waves is described by (2.12).

Eq. (2.12) contains 4 unknown energy sources: a background zonal electric field, a zonal polarization electric field written in terms of the current velocity u_{0x}, meridional and zonal neutral winds. The relative plasma density fluctuation of the primary wave in Eq. (2.12) isn't known either, although a reasonably good guess can be made based on evidence and simulation. We will discuss this point in more detail below. We use the term background for the zero-order electric field meaning that its typical scale-length is much larger than the typical scale of the polarization electric field produced by the primary waves.

Let's have a detailed look at the right-hand side (RHS) of Eq. (2.12). The zonal neutral wind in the last term in the braces has the coefficient q_i compared to the meridional wind. For the lower E region q_i <<1 and the contribution from the zonal wind can be neglected compared to that from the meridional wind. For the higher E region ions become magnetized and q_i >1, or even >>1. In this case the zonal wind will dominate in the third term in Eq. 2.12, but the coefficient of the whole term becomes very small: ψ/q_i <<1. Even for q_i =1, which for the MU radar corresponds to the altitudes 130-135 km, $\psi \approx 10^{-4}$. Obviously, at these altitudes there does not exist a neutral wind capable of contributing noticeably to the phase velocity. Thus, this term noticeably contributes to the phase velocity only in the lower E region by means of the meridional neutral wind. Above about 102 km the neutral wind doesn't affect the phase velocity.

Note also the polarization electric field (the second term in braces on RHS) decreases with increasing ion magnetization (increasing height) and the large-scale electric field defines the phase velocity above 120 km altitude. The abovementioned peculiarities are seen in Fig. 2, in which we have plotted the coefficients of each of the three RHS terms in Eq. 2.12.

Going down in altitude q_i decreases. Below approximately 94-96 km this results in $\psi > 1$ and the second and third terms in braces dominate the line-of-sight phase velocity. It can be seen also from Fig. 2 where below 94 km the contribution from the background electric field becomes negligible.

Thus the line-of-sight phase velocity at almost any altitude in the E region is defined by only two contributors.

The major part of E-region backscatter has been observed below 125 km. For the lower E region we may assume $q_i < 1$ (which implies $q_i^2 << 1$ and so allows us to neglect q_i^2 in comparison with 1) and rewrite (1) as:

$$V_{ph,\mathrm{sec},y} = C_{E0x}E_{0x}/B_0 + C_{u0x}u_{0x} + C_{uny}u_{ny}, \quad (3.1)$$

where

$$C_{E0x} = \frac{1}{1+\psi};\ C_{u0x} = \frac{n_{pr}}{q_i(1+\psi)^2};\ C_{uny} = \frac{\psi}{1+\psi}. \quad (3.2)$$

Now the left-hand side (LHS) of (3.1) is the measured line-of-sight Doppler velocity, and the right-hand side of (3.1) is a sum of contributions to the secondary gradient drift instability (GDI) written in terms of velocity. From left to right these contributors are: a large-scale "background" electric field (large scale in the sense that its typical scale-length is much more than the typical scale-length of the polarization electric field caused by the primary waves), a polarization electric field due to primary waves, and a line-of-sight neutral wind. Note that all three

contributions to the RHS of Eq. 3.1 are unknown although at almost any altitude in the E region (as we have shown) only two of them define the line-of-sight phase velocity.

Note that the coefficients C_j are functions of local time, place and altitude and may be calculated for the time and location of each observational data set.

In Fig. 2 we plot the dimensionless coefficients C_j of each contribution (the RHS terms in Eqs. 2.12 and 3.1) to the phase velocity (the LHS term in Eq. 3.1) as a function of altitude for the general case of arbitrary ion magnetization. The phase velocity has the coefficient C_{Vph}=1. In calculating C_{u0x} we have assumed $n_{pr} = 5\%$. We explain our reasons for this assumption in the end of Subsection 3.2.2. From Fig. 2 it can clearly be seen that all coefficients C_j change rapidly with altitude due to the exponential altitude dependence of the collisional frequencies, but each exhibits a very different altitude behavior.

Figure 2

In Fig. 2 the magnitudes of the electron and ion collisional frequencies in C_j were calculated using the formulas in *(Schunk and Nagy,* 2000). The neutral densities and electron/ion temperature in the formulas for collisional frequencies (T_e=T_i=T_n for the altitudes of interest) were calculated using the MSIS-E-90 model (*Hedin,* 1991). All quantities were calculated for the MU-radar experiment on October 1, 2001 (Shigaraki, Japan, 34.9°N, 136.1°E) for the time 10:00 pm. The gyro frequencies were calculated in accordance with the geomagnetic field data from the IGRF model. Both models (MSIS-E-90 and IGRF) may also be found on the National Space Satellite Data Center web site http://nssdc.gsfc.nasa.gov/space/model/.

From Fig. 2 it follows that for this given time and location: (1) the polarization electric field due to primary waves by itself defines the phase velocity near 98-102 km altitude ($C_{u0x} >> C_{u0y}, C_{E0x}$); (2) at altitudes of 90-94 km the contribution from the background electric field is negligible compared to that of neutral winds and the polarization electric field; and (3) above about 115 km the background electric field dominates the phase velocity. It can be seen that C_{E0x} decreases with altitude starting from 120 km, since the ions become more and more magnetized (the ion-neutral collisional frequency drops exponentially with altitude) and drift together with the electrons in crossed $E \times B$ when $\omega_i >> \nu_{in}$.

3.2. Basis of the Method

3.2.1. Boundary condition.

Next we are going to apply our preliminary knowledge of the E-region processes. In accordance with E-region backscatter observations our principal interest is in the altitude range 90-120 km. *Larsen* (2002) has catalogued and analyzed over 400 neutral wind profiles collected since 1958. He has shown that at middle and low latitudes the wind velocity is maximum in the altitude range between l00 and 110 km and the maximum wind velocity has exceeded l00 m/s in 60% of the observations. The maximum speed ever observed was between 160 and 170 m/s. Based on Larsen's analysis of wind data (*Larsen,* 2002) one may postulate $u_n \leq 170$ m/s.

Based on the fact that the coefficients in Eq. 3.1 have very different altitude dependences (Fig. 2) we will use the C_j as filters in the following. Let's suppose for a moment that only one of the contributions in the RHS of Eq. 3.1 defines the phase velocity (LHS of Eq. 3.1) and calculate from the Doppler data and Eqs. (3.1) and (3.2) what this phase velocity for each separate contributor would be if this were the case. To this end

we calculate C_j in accordance with the scheme described above for the time and location corresponding to the time and location of each set of the Doppler measurements analyzed.

We plot C_j in Fig. 3a and the observed phase velocity, the meridional neutral wind, and the zonal large-scale and polarization electric fields for this hypothesized case in Fig. 3b for the MU radar observations at the time 2:50:05.9 LT on July 25, 2001. In Fig. 3b we show these supposed velocities as thin lines and mark in gray the area (confined by the dashed white lines) to indicate the observable velocity range ±170 m/s. These white dashed lines show the maximum possible amplitude of wind velocities which have ever been observed in connection with type-2 backscatter at E-region equatorial and middle latitudes (*Larsen,* 2002).

Figure 3

From Fig. 3 we see that there are altitude ranges where the filter velocities have magnitudes which have never been observed. This fact allows us to discard at some definite altitude those contributions whose velocity significantly exceeds 170 m/s (the white dashed line in Fig. 3). In doing so we use the coefficients C_j as filters which allow us to find the altitude(s) at which only one contributor defines the phase velocity. For the data in Fig. 3 it is the polarization electric field near 99 km altitude. Thus, we have found the boundary condition for the driving forces of the instability. The procedure has been repeated for each altitude profile of the phase velocity of the secondary waves.

The boundary condition is the basic starting point of our method. As a rule for almost any backscatter event in the E region at least one boundary condition exists. Near 100 km altitude it is as a rule for the polarization electric field as in the example discussed above. Above about 116 km the boundary condition is for the large-scale electric field. Near 94 km and below it is for the neutral wind.

Note, that the boundary condition is absolutely essential for the following procedure if we don't know the magnitude of any of the contributors to the line-of-sight phase velocity from measurements. In cases when one of these contributors is known (for example the large-scale electric field measured in the F region and mapping down to the E region) this fact can be used as a boundary condition (in our example for the altitudes above 100 km).

3.2.2. Reconstruction of winds and electric fields.

In the following we are going to use the boundary condition for reconstruction of neutral winds and electric fields. For each backscatter observation time (for the MU radar the time resolution may be as small as several seconds), we have ***a data set of Doppler velocities*** from the backscatter altitudes with an altitude step $\Delta\zeta$ (the altitude resolution of the radar) ***and the boundary condition at the altitude*** $\zeta 1$. We assume that the altitude resolution of the radar is good enough to consider ***the energy sources*** (neutral winds and electric fields) to be ***the same for two neighboring altitudes of observation***. This assumption defines the resolution of our method and one has to decide if this altitude/time resolution is acceptable for his or her purposes.

In the following we demonstrate the data-processing procedure for the case when we have the boundary condition at the altitude $\zeta 1$ (99 km for the data set in Fig. 3b) for the zonal polarization electric field written in terms of the current velocity $u_{0x}^{\zeta 1}$ (Eq. 3.1). We then go step-by-step down (up) in altitude assuming that at the neighboring altitude $\zeta 1-\Delta\zeta$ ($\zeta 1+\Delta\zeta$) the current velocity remains the same: $u_{0x}^{\zeta 1} = u_{0x}^{\zeta 1-\Delta\zeta}$.

As we have discussed above, from Fig. 2 it follows that, as a rule, at any given altitude the phase velocity is defined by no

more than two contributors. This gives us two equations for phase velocities (in the following we omit subindices *sec,y*), $V_{ph}^{\zeta 1}$ and $V_{ph}^{\zeta 1-\Delta\zeta}$ at two neighboring altitudes with coefficients $C_i^{\zeta 1}$ and $C_i^{\zeta 1-\Delta\zeta}$, and two unknowns $u_{0x}^{\zeta 1}$ and $u_{ny}^{\zeta 1-\Delta\zeta}$, respectively. As we have mentioned above the coefficients $C_i^{\zeta 1}$ and $C_i^{\zeta 1-\Delta\zeta}$ (found from models for the time and location of the experiments) are fast-changing with altitude and noticeably different at two neighboring altitudes separated by the radar height resolution. Evaluating $u_{0x}^{\zeta 1}$ from Eq. 3.1 for $V_{ph}^{\zeta 1}$

$$u_{0x}^{\zeta 1} = V_{ph}^{\zeta 1} / C_{u0x}^{\zeta 1}, \tag{3.3}$$

we then substitute it into Eq. 3.1 for $V_{ph}^{\zeta 1-\Delta\zeta}$, from which we now can find the other contributor (for this particular case, the meridional neutral wind velocity $u_{ny}^{\zeta 1-\Delta\zeta}$):

$$u_{ny}^{\zeta 1-\Delta\zeta} = \left(V_{ph}^{\zeta 1-\Delta\zeta} - V_{ph}^{\zeta 1} \frac{C_{u0x}^{\zeta 1-\Delta\zeta}}{C_{u0x}^{\zeta 1}} \right) \Bigg/ C_{uny}^{\zeta 1-\Delta\zeta}. \tag{3.4}$$

Then we assume that for the altitude one step down, $\zeta 1–2\Delta\zeta$, the meridional wind remains the same:

$$u_{ny}^{\zeta 1-\Delta\zeta} = u_{ny}^{\zeta 1-2\Delta\zeta}. \tag{3.5}$$

This allows us to find the polarization electric field at the altitude $\zeta 1–2\Delta\zeta$ from Eq. 3.1 for $V_{ph}^{\zeta 1-2\Delta\zeta}$:

$$u_{0x}^{\zeta 1-2\Delta\zeta} = \left\{ V_{ph}^{\zeta 1-2\Delta\zeta} + \frac{C_{uny}^{\zeta 1-2\Delta\zeta}}{C_{uny}^{\zeta 1-\Delta\zeta}} \times \left[-V_{ph}^{\zeta 1-\Delta\zeta} + \frac{C_{uny}^{\zeta 1-\Delta\zeta}}{C_{uny}^{\zeta 1}} V_{ph}^{\zeta 1} \right] \right\} \Bigg/ C_{u0x}^{\zeta 1-2\Delta\zeta}, \tag{3.6}$$

and so on.

Note that going up in altitude from the boundary condition with a step $\Delta\zeta$ (altitude resolution of the radar) and applying the same scheme allows reconstruction of the zonal large-scale (E_{0x}) and polarization ($u_{0x}B_0$) electric fields. Written in terms of velocity they are:

$$E_{0x}^{\zeta 1+\Delta\zeta} / B_0 = \left(V_{ph}^{\zeta 1+\Delta\zeta} - V_{ph}^{\zeta 1} \frac{C_{u0x}^{\zeta 1+\Delta\zeta}}{C_{u0x}^{\zeta 1}} \right) \Bigg/ C_{E0x}^{\zeta 1+\Delta\zeta}, \tag{3.7}$$

$$E_{0x}^{\zeta 1+\Delta\zeta} = E_{0x}^{\zeta 1+2\Delta\zeta}, \tag{3.8}$$

$$u_{0x}^{\zeta 1+2\Delta\zeta} = \left\{ V_{ph}^{\zeta 1+2\Delta\zeta} + \frac{C_{E0x}^{\zeta 1+2\Delta\zeta}}{C_{E0x}^{\zeta 1+\Delta\zeta}} \times \left[-V_{ph}^{\zeta 1+\Delta\zeta} + \frac{C_{E0x}^{\zeta 1+\Delta\zeta}}{C_{E0x}^{\zeta 1}} V_{ph}^{\zeta 1} \right] \right\} \Bigg/ C_{u0x}^{\zeta 1+2\Delta\zeta} \tag{3.9}$$

It should be mentioned that with each subsequent step down/up in altitude the uncertainty of the method will grow. It is possible to diminish this increasing error in cases when backscatter is observed over a wide altitude range and the data allow us to find two or more boundary conditions, *i.e.* for the

data sets in which there are two or more altitudes where only one contributor defines the phase velocity. Then the contributions may be found using a combination of upward and downward step-by-step evaluation as described above with the obligatory match to the clear boundary condition.

Obviously the above procedure can't be used if backscatter comes only from altitudes where two contributors are equally important, since otherwise we would not be able to find the boundary condition.

In reconstructing the neutral winds and electric fields, we calculate each of the coefficients $C_j^{\zeta 1 \mp s\Delta\zeta}$, where s = 1, 2, 3, ..., for the time and location of each backscatter event using the altitude dependences of the collisional and gyro frequencies, which we have found from formulas and the MSIS-E-90 and IGRF models.

Finally, we have had to make some assumptions on the primary waves. Since our method is based on the expression for the line-of-sight Doppler velocity which, unlike the signal power (*Hocking,* 1985), doesn't depend on the primary wave spectrum, the polarization electric field is influenced only by the relative density fluctuation in the primary wave but not the primary turbulence scale. Based on observations at middle and equatorial latitudes, we suppose that this relative plasma density fluctuation in the primary wave n_{pr} is 5%. We think that this assumption is reasonable, since numerical studies by *McDonald et al.* (1975) showed that the generation of secondary small-scale gradient-drift irregularities with λ<28 m were excited when the amplitude of the larger-scale primary waves exceeded 4% of the background plasma density. Also midlatitude rocket observations (*Bowhill,* 1966; *Itoh et al,.* 1975; and *Kelley et al,,* 1995) showed that n_{pr} was correspondingly 5-10%, 1-5% and 7%.

Note, that the reconstruction procedure assumes that n_{pr} is constant. In fact there is a possibility that n_{pr} may vary along the radar line-of-sight (several ionization clouds in the radar field-of-view). Since C_{u0x} is assumed constant for the given altitude and time, in the case of variations of n_{pr} along the radar line-of-sight relative to the supposed n_{pr}^0 =5%, our method will produce a sinusoidally-modulated polarization electric field. In fact, it is possible that precisely this very rare case of three ionization clouds can be seen in the altitude range 100-103 km near 2:53 AM LT (Section 4, Case Study; left upper and middle panels in Fig. 5).

3.2.3. Requirements of the method.

Summing all the above, we may formulate the necessary conditions for the use of the proposed method as follows:

- in the backscatter data there should be at least one altitude at which only one contributor defines the phase velocity (the boundary condition);
- the coefficients *Cj* change with altitude fast enough to be noticeably different at two neighboring altitudes separated by the altitude resolution of the radar;
- backscatter should be observed from at least 3 neighboring altitudes;
- the altitude resolution of the radar should be good enough to provide reasonable resolution of the winds and electric fields.

4. Case Study

We apply our method to the backscatter Doppler velocities observed on the night of July 25, 2001 with the MU radar over Shigaraki, Japan (34.9°N, 136.1°E; geomagnetic latitude 25.0°N). Backscatter from field-aligned irregularities was observed throughout almost the entire night. In Fig. 4 we present a portion of these data for the time period 2:20 – 3:30 am LT. In Fig. 4 we show the line-of-sight Doppler velocity V_{Dop} as a function of local time for different altitudes shown in different colors. Here positive Doppler velocities are away from the radar, i.e. in the *-y* direction. The sudden splashes in the Doppler velocity at about 2:52 LT near 94.8 km altitude and at about 2:58 LT near 107.2 km altitude (see also the two upper panels in Fig. 5) are most probably caused by meteors. The Doppler velocity was mainly away from the radar except for the time period from about 2:40 LT until about 3:08 LT when it was towards the radar. To demonstrate the method we chose 14 consecutive time data sets during the period of the "inverse" Doppler velocity from 2:50:06 until 2:59:40 LT (the phase velocity as a function of local time and altitude is presented in the two upper panels in Fig. 5). We analyzed only the data for which the signal-to-noise ratio (SNR) exceeds 3 dB. The major part of the data has SNR> 21 dB.

Figure 4

In Fig. 5 we plot together the observed phase velocities of the 3.2-m irregularities and the derived polarization electric field (written in terms of the current velocity) and neutral wind. The left column presents the altitude profiles of the phase velocity (upper panel), the reconstructed current velocity (middle panel) and the reconstructed meridional neutral wind (lower panel) for different local times, and the right column shows the time history of the phase velocity (upper panel), the reconstructed current velocity (middle panel) and the reconstructed meridional neutral wind (lower panel) at different altitudes. To show the trend we connect consecutive data points by smooth lines for both the phase velocity and reconstructed parameters.

Figure 5

The altitude dependence of the reconstructed zonal polarization electric field in the middle left panel of Fig. 5 shows sinusoidal behavior for 2:50:50.0 LT between 96.2 and 98.2 km altitudes and for 2:53:02.9 LT between 100.2 and 102.2 km altitudes with the same height period of approximately 670 m. The zonal polarization electric field at these altitudes is due to ion drag by the zonal neutral wind and electron drift in the crossed background meridional electric and geomagnetic fields (Eq. 2.12). Since the background electric field by definition has a much larger typical scale-length, the observed sinusoidal altitude dependence is due to either the zonal wind or the plasma density fluctuation n_{pr} in the primary wave, which we have assumed constant (Eqs. 3.1 and 3.2).

The reconstructed altitude profiles at consecutive times and time histories at consecutive altitudes for the meridional neutral wind are plotted in the lower panels of Fig. 5. The splashes of the wind velocity near 2:51 am LT are due to distortion of the Doppler velocities by meteors.

Note that our method allows the reconstruction of the meridional wind velocity up to about 100 km altitude (in some cases up to 102-103 km). Then, with increasing altitude the coefficient of the wind velocity decreases rapidly (see Fig. 2) and at 108-110 km becomes so small that observed winds couldn't provide any noticeable contribution to the phase velocity in Eq. 3.1.

The large-scale electric field may be reconstructed for altitudes above 100 km. We found that the magnitude of the background zonal electric field was about – (0.2-0.5) mV/m. During 2:50:05.9- 2:52:18.6 LT the reconstruction shows a zonal electric field of up to about –4 mV/m in the 100-104 km altitude

range. This large-scale (about 4 km) electric field is most probably a polarization electric field for the primary waves caused by a large-scale ionization cloud which appeared in the radar field-of-view.

5. Discussion and Conclusions

We have described a technique to observe the neutral winds and electric fields with backscatter from field-aligned irregularities in the E region. The method doesn't require additional expense and may be used at any ISR whose altitude resolution is one half of the least allowable resolution of the energy sources: neutral winds and electric fields.

There are two basic ideas at the heart of our method. The first is that the expression of the phase velocity is, to leading order, the same as for linear processes, independently of the degree of nonlinearity of the actual mechanism causing the small-scale irregularities. The second is that coefficients at each contributor to this phase velocity are fast changing with altitude and show quite different altitude behavior. The second idea allows us to use these coefficients as filters to find the boundary condition, i.e. the altitude(s) at which only one contributor defines this phase velocity.

Showing that at almost any altitude there are only two contributors dominating the phase velocity, we assume the driving forces for the 3-m waves to be alternately the same at two neighboring altitudes separated by the altitude resolution of the radar. Finally, based on modeling and observations we have assumed the relative density fluctuation in the primary wave to be 5%.

The above scheme allows us reconstruction of winds and electric fields from the altitude-time distribution of line-of-sight Doppler velocities over the altitude range covered by backscatter with type-2 spectral signature with altitude and time resolutions which are equal to twice the altitude resolution and equal to the temporal resolution of the radar measurements, respectively.

Our method allows reconstruction of:

- the meridional neutral wind up to 100 km,
- the zonal polarization electric field caused by the primary waves (driven by the meridional electric field and the zonal neutral wind) up to 120 km,
- the background zonal electric field above 100 km.

We made an attempt to compare the wind velocities derived by our method with the meteor radar data available for the same time and location. However, despite the fact that the time near 3 am was the period of the highest meteor occurrence, the time and height resolution of the meteor radar for the time of interest were 2 hours and 2 km, respectively.

It should be mentioned that, like other wind-measuring methods, our method smoothes shears in the neutral wind to the scale of the altitude resolution of the method. The best resolution in the wind measurements is provided by *in situ* measurements with the chemical release technique. It allows an altitude resolution of about 100 m (*Larsen,* 2002). For remote observations with meteor radar, the altitude resolution depends on the number of meteors and, as we have already mentioned, for the case study above it was 2 km. Note that a large shear in the wind velocity in the lower E region results in sporadic ionization with a typical vertical scale of the sporadic layer (E_s) equal to the shear vertical scale-length. Observations yield E_s vertical scales L=1-2 km as a rule, with occasionally L=500 m and rare cases of a very complex structure of the underlying ionization clouds (*Bakhmet'eva et al.*, 2003). Thus, we don't expect to lose much information if any about the neutral winds.

Note that our method is based on the expression for the phase velocity along the radar line-of-sight. In our description above and in correspondence to most of the observations, we assume that the radar observes in the meridional plane. If the CSR line-of-sight isn't in the meridional plane, then the most general expression (2.13) should be used. It is important that, independently of the complexity of the processes generating small-scale irregularities (gradient-drift, thermal or Farley-Buneman), the expression for the phase velocity/frequency, to leading order, is the same. However, we remind once more, that one should keep in mind that our method is valid only for irregularities producing type-2 backscatter whose phase speed is less then the ion acoustic speed ($V_{Dop} < c_s$).

It should be mentioned that for the correct range-to-altitude conversion the preliminary radar imaging technique *[Kudeki and Siiriicii,* 1991; *Woodman,* 1997; *Hysell and Burcham,* 2000; *Hysell et al.,* 2002] should be used when possible for more correct altitude profiles of the Doppler line-of-sight velocity.

Acknowledgments. The authors acknowledge useful discussions with Dave Hysell. The work of one of the authors (LMK) has been supported in part by the Russian Foundation of Basic Research grants 01-05-65025 and 02-05-65281 and by the Canadian Natural Sciences and Engineering Research Council. The MU radar belongs to and is operated by the Radio Science Center for Space and Atmosphere (RASC) of Kyoto University. LMK was supported by RASC as a visiting scientist during the preparation of this manuscript.

References

Bakhmet'eva, N.V., V.V. Belikovich, L.M. Kagan, and A.A. Poniatov, Formation and dynamics of sporadic E layers throughout sunset-to-sunrise hours (new results), Summary of Presentations, RF Ionospheric Interactions Workshop, v.2, 699-714, 2003.

Bowhill, S.A., A rocket experiment on the structure of sporadic E, *Radio Sci,. 1,* 187-190, 1966.

Buneman, O., Excitation of field-aligned sound waves by electron streams, *Phys. Rev. Lett., 10,* 285, 1963.

Cosgrove, R. B. and R.T. Tsunoda, Polarization electric fields sustained by closed-current dynamo structures in midlatitude sporadic E, *Geophys. Res. Lett.*, *28* , 1455, 2001.

Dimant, Y.S. and R.N. Sudan, Physical nature of a new cross-field current-driven instability in the lower ionosphere, *J. Geophys. Res.*, *102*, 2551, 1997.

Dimant, Y. S. , and M. M. Oppenheim, Ion thermal effects on E-region instabilities: linear theory, *J. Atmos. Solar-Terr. Phys.,* 2003, in press.

Farley, D.T., Two-stream plasma instability as a source of irregularities in the ionosphere, *Phys. Rev. Lett., 10*, 217, 1963.

Fejer, B.G., and M.C. Kelley, Ionospheric irregularities, *Rev. Geophys. Space Phys., 18,* 401, 1980.

Fukao, S., M. Yamamoto, R.T. Tsunoda, H. Hayakawa, and T. Mukai, The SEEK (Sporadic-E experiment over Kyushu) campaign*, Geophys. Res. Lett., 25*, 1761-1764, 1998.

Hedin, *J. Geophys. Res.*, *96*, 1159-1172, 1991.

Hocking, W.K., Measurements of turbulent energy dissipation rates in the middle atmosphere by radar techniques: A review, *Radio Sci.,20(6),* 1403-1422, 1985.

Hocking, W.K., Recent advances in radar instrumentation and techniques for studies of the mesosphere, stratosphere and troposphere, *Radio Sci., 32,* 2241-2270, 1997.

Hocking, W.K., B. Fuller, and B. Vandepeer, Real-time determination of meteor-related parameters utilizing modern digital technology, *J. Atmos. Solar-Terr. Phys., 63*, 155-169, 2001.

Hysell, D. L., and J. Burcham, The 30 MHz radar interferometer studies of midlatitude *E* region irregularities, *J. Geophys. Res.*, *105*, 12,797, 2000.

Hysell, D. L., M. Yamamoto, and S. Fukao, Imaging radar observations and theory of type I and type II quasiperiodic echoes , *J. Geophys. Res.*, *107(A11)*, 2002.

Jacka, F., Application of Fabry-Perot Spectrometers for Measurement of Upper Atmosphere Temperatures and Winds, *Middle Atmosphere Program, Handbook for MAP, 13*, 19-40, 1984.

Itoh, T., M. Nakamura, and Y. Nakamura, Rocket observations of electron density irregularities in the middle latitude E region, *Geophys. Res. Lett., 2,* 553-555, 1975.

Kagan, L.M. and M.C.Kelley, A wind-driven gradient drift mechanism for mid-latitude E-region ionospheric irregularities, *Geophys. Res. Lett., 25*, 4141-4144, 1998.

Kagan, L.M. and M.C.Kelley, A thermal mechanism for generation of type-2 small-scale irregularities in the ionospheric E region, *J. Geophys. Res., 105*, 5291-5303, 2000.

Kagan, L.M., T.Ogawa, S.Fukao and M.Yamamoto, A role of neutral motions in formation of midlatitude E-region field-aligned irregularities, *Geophys. Res. Lett., 27*, 939-942, 2000.

Kagan, L.M., Effects of neutral gas motions on midlatitude irregular structure, *J. Atmos. Sol. Terr. Phys. (ISEA-10 special issue),* ***64***, 1479-1486, 2002.

Kelley, M.C., The Earth Ionosphere: Plasma Physics and Electrodynamics, *43, International Geophysical Series,* Academic Press, NY, 1989.

Kelley, M.C., D. Riggin, R.F. Pfaff, W.E. Swartz, J.F. Providakes, and C.-S. Huang, Large amplitude quasi-periodic fluctuations associated with a mid-latitude sporadic E-layer, *J. Atmos. Terr. Phys., 57*, 1165, 1995.

Kudeki, E., and F. Sürücü, Radar interferometric imaging of field-aligned plasma irregularities in the equatorial electrojet, *Geophys. Res. Lett.*, *18*, 41, 1991.

Larsen, M.F., S. Fukao, M. Yamamoto, R. Tsunoda, K. Igarashi, and T. Ono, The SEEK chemical release experiment: Observed neutral wind profile in a region of sporadic-E, *Geophys. Res. Lett., 25,* 1789-1792, 1998.

Larsen, M.F., Winds and shears in the mesosphere and lower thermosphere: results from four decades of chemical release wind measurements, *J. Geophys. Res., 107(A8),* 2002.

McDonald, B.E., T.P. Coffey, S.L. Ossakow, and R.N. Sudan, Numerical studies of type 2 equatorial electrojet irregularity development, *Radio Sci., 10,* 247, 1975.

Murthy, B.V.K., S. Ravindran, K.S. Viswanathan, and K.S.V. Subbarao, A.K. Patra, and p.b. Rao, Small-scale (~3 m) E region irregularities at and off the magnetic equator, *J. Geophys. Res., 103(A9),* 20,761-20,772, 1998.

Patra, A.K., On the interpretationof the VHF radar echoes from the equatorial lower E region, *Geophys. Res, Lett, 29(14)*, 2002.

Pfaff, R., M. Yamamoto, P. Marionni, H. Mori, and S. Fukao, Electric field measurements above and within a sporadic E layer, *Geophys. Res. Lett., 25,* 1769-1772, 1998.

Roper, R.G., MWR – Meteor Wind Radars, *Middle Atmosphere Program, Handbook for MAP, 13*, 124-134, 1984.

Rottger, J., The MST radar technique, *Middle Atmosphere Program, Handbook for MAP, 13*, 187-232, 1984.

Rogister, A. and N. D'Angelo, Type II irregularities in the equatorial electrojet, *J. Geophys. Res., 75,* 3879, 1970.

Schunk, R.W., and A.F. Nagy, *Ionospheres: Physics, Plasma Physics, and Chemistry,* Atmospheric and Space Science Series, Cambridge University Press, 2000.

Shepherd, G.G., et al., WINDII, the Wind Imaging Interferometer on the Upper Atmosphere Research satellite, *J. Geophys. Res., 98,* 10725-10750, 1993.

Sudan, R.N., J. Akinrimisi, and D.T. Farley, Generation of small-scale irregularities in the equatorial electrojet, *J. Geophys. Res., 78,* 240, 1973.

Sudan, R.N., Unified theory of type I and type II irregularities in the equatorial electrojet, *J. Geophys. Res.*, *88*, 4853, 1983.

Tsunoda, R.T., and W.L. Ecklund, On the nature of the radar echoes below 95 km during counter streaming in the equatorial electrojet, *Geophys. Res. Lett., 26,* 2717, 1999.

Woodman, R. F., Coherent radar imaging: Signal processing and statistical properties, *Radio Sci.*, *32*, 2373, 1997.

Yokoyama, T., M. Yamamoto, and S. Fukao, Computer simulation of polarization electric field as a source of midlatitude field-aligned irregularities, *J. Geophys. Res., 108(A2),* 1054, doi: 10.1029/2002 JA009513, 2003.

Yokoyama, T., M. Yamamoto, S. Fukao, and R. B. Cosgrove, Three-Dimensional Simulation on Generation of Polarization Electric Field in the Midlatitude E-Region Ionosphere, *J. Geophys. Res., 109(A1),* 309, doi: 10.1029/2003JA010238, 2004.

L.M. Kagan[1,2], S. Fukao, and M. Yamamoto, Radio Science Center for Space and Atmosphere, Kyoto University, Japan. . (lkagan@uwo.ca; fukao@rish.kyoto-u.ac.jp; yamamoto@rish.kyoto-u.ac.jp)
P.B. Rao, National Remote Sensing Agency, Department of Space Balanagar, Hyderabad 500 037, AP, India (rao_pb@nrsa.gov.in).

Figure Captions

Figure 1. A Cartesian coordinate system related to the routine observational geometry of most coherent scatter radars.

Figure 1. A Cartesian coordinate system related to the routine observational geometry of most coherent scatter radars.

Figure 2. The dimensionless coefficients Cj of each contribution to the phase velocity as a function of altitude calculated for 10:00 pm on October 1, 2001, Shigaraki, Japan, 34.9°N, 136.1°E.

Figure 2. The dimensionless coefficients Cj of each contribution to the phase velocity as a function of altitude calculated for 10:00 pm on October 1, 2001, Shigaraki, Japan, 34.9°N, 136.1°E.

Figure 3. a). The coefficients (filters) C_j calculated for the MU radar backscatter observed in the 94-106.4 km altitude range at 2:50-3:00 am on July 25, 2001; b). Illustration of the finding of a boundary condition by applying the filters from Fig. 3a. The phase velocity observed with the MU radar at 2:50:05.9 LT on July 25, 2001 is shown by the thin black line with rhombuses. The meridional neutral wind, the zonal large-scale and polarization electric fields calculated in terms of velocity for the hypothesized case when only one contributor defines the phase velocity are marked by thin black, gray and white lines correspondingly. The meridional neutral wind, the zonal large-scale and polarization electric fields reconstructed for the MU radar observations at 2:50:05.9 LT on July 25, 2001 are shown by thick black, gray and white lines correspondingly. The gray area confined by the dashed white lines, indicate the observable velocity range ±170 m/s. The dashed-line rounded rectangle indicates the altitude range over which the only one contributor (the polarization electric field in this particular case) defines the phase velocity observed.

Figure 3. a). The coefficients (filters) C_j calculated for the MU radar backscatter observed in the 94-106.4 km altitude range at 2:50-3:00 am on July 25, 2001; b). Illustration of the finding of a boundary condition by applying the filters from Fig. 3a. The phase velocity observed with the MU radar at 2:50:05.9 LT on July 25, 2001 is shown by the thin black line with rhombuses. The meridional neutral wind, the zonal large-scale and polarization electric fields calculated in terms of velocity for the hypothesized case when only one contributor defines the phase velocity are marked by thin black, gray and white lines correspondingly. The meridional neutral wind, the zonal large-scale and polarization electric fields reconstructed for the MU radar observations at 2:50:05.9 LT on July 25, 2001 are shown by thick black, gray and white lines correspondingly. The gray area confined by the dashed white lines, indicate the observable velocity range ±170 m/s. The dashed-line rounded rectangle indicates the altitude range over which the only one contributor (the polarization electric field in this particular case) defines the phase velocity observed.

Figure 4. The line-of-sight Doppler velocity V_{Dop} observed with the MU radar as a function of local time for different altitudes shown in different colors (the night of July 25, 2001, Shigaraki, Japan).

Figure 4. The line-of-sight Doppler velocity V_{Dop} observed with the MU radar as a function of local time for different altitudes shown in different colors (the night of July 25, 2001, Shigaraki, Japan).

Figure 5. The observed phase velocities of the 3.2-m irregularities and the derived polarization electric field written in terms of the current velocity. The left column presents the altitude profiles of the phase velocity (upper panel), the reconstructed current velocity (middle panel) and the meridional neutral wind velocity (lower panel) for different local times, and the right column shows the time history of the phase velocity (upper panel), the reconstructed current velocity (middle panel) and the meridional neutral wind velocity (lower panel) at different altitudes (the night of July 25, 2001, Shigaraki, Japan).

Figure 5. The observed phase velocities of the 3.2-m irregularities and the derived polarization electric field written in terms of the current velocity. The left column presents the altitude profiles of the phase velocity (upper panel), the reconstructed current velocity (middle panel) and the meridional

neutral wind velocity (lower panel) for different local times, and the right column shows the time history of the phase velocity (upper panel), the reconstructed current velocity (middle panel) and the meridional neutral wind velocity (lower panel) at different altitudes (the night of July 25, 2001, Shigaraki, Japan).

KAGAN ET AL.: E-REGION WINDS AND ELECTRIC FIELDS

KAGAN ET AL.: E-REGION WINDS AND ELECTRIC FIELDS

KAGAN ET AL.: E-REGION WINDS AND ELECTRIC FIELDS

KAGAN ET AL.: E-REGION WINDS AND ELECTRIC FIELDS

KAGAN ET AL.: E-REGION WINDS AND ELECTRIC FIELDS

KAGAN ET AL.: E-REGION WINDS AND ELECTRIC FIELDS

KAGAN ET AL.: E-REGION WINDS AND ELECTRIC FIELDS

KAGAN ET AL.: E-REGION WINDS AND ELECTRIC FIELDS

KAGAN ET AL.: E-REGION WINDS AND ELECTRIC FIELDS

KAGAN ET AL.: E-REGION WINDS AND ELECTRIC FIELDS

KAGAN ET AL.: E-REGION WINDS AND ELECTRIC FIELDS

KAGAN ET AL.: E-REGION WINDS AND ELECTRIC FIELDS

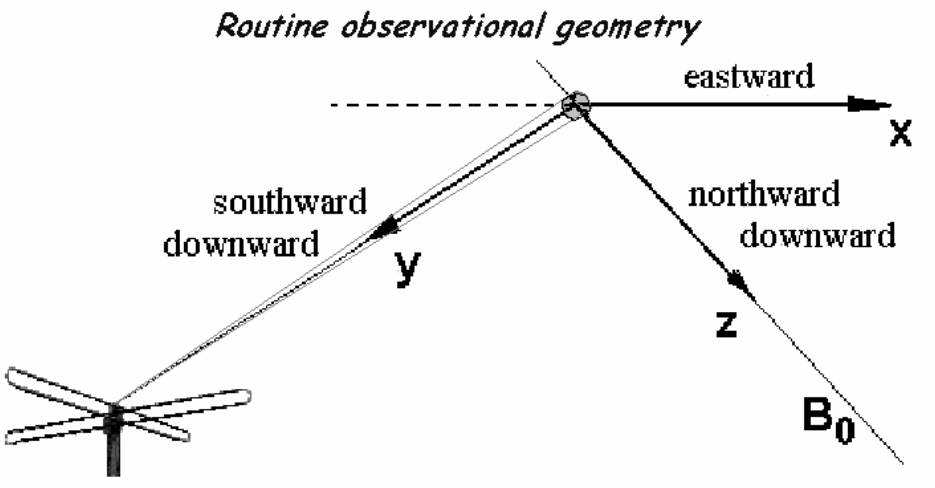
Routine observational geometry
eastward
x
southward
downward
y
northward
downward
z
B0

Fig. 1

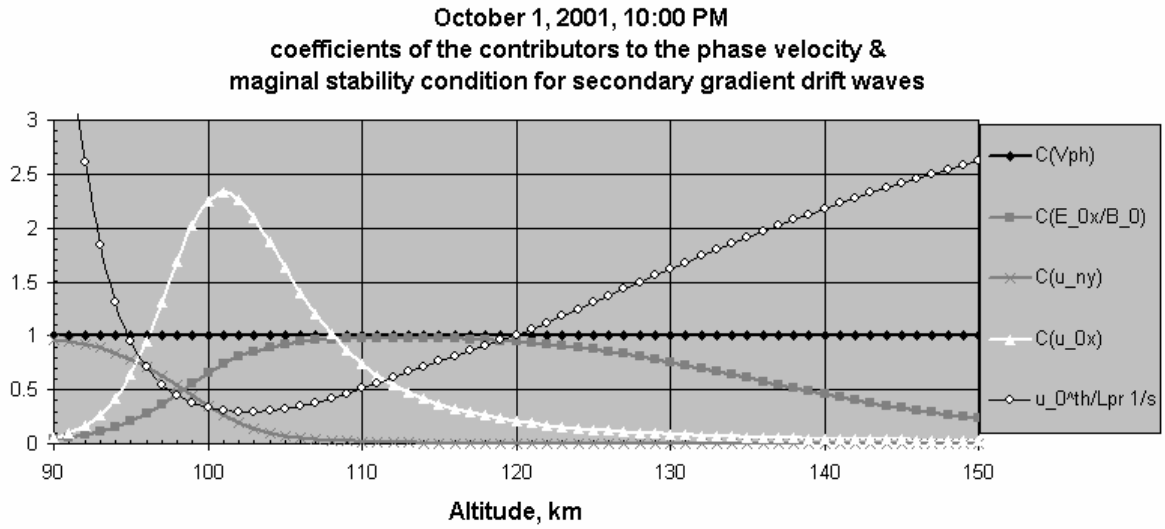
October 1, 2001, 10:00 PM
coefficients of the contributors to the phase velocity &
maginal stability condition for secondary gradient drift waves
3
2.5
2
1.5
1
0.5
0
90
100
110
120
130
140
150
Altitude, km
C(Vph)
C(E_0x/B_0)
C(u_ny)
C(u_0x)
u_0^th/Lpr 1/s

Fig. 2

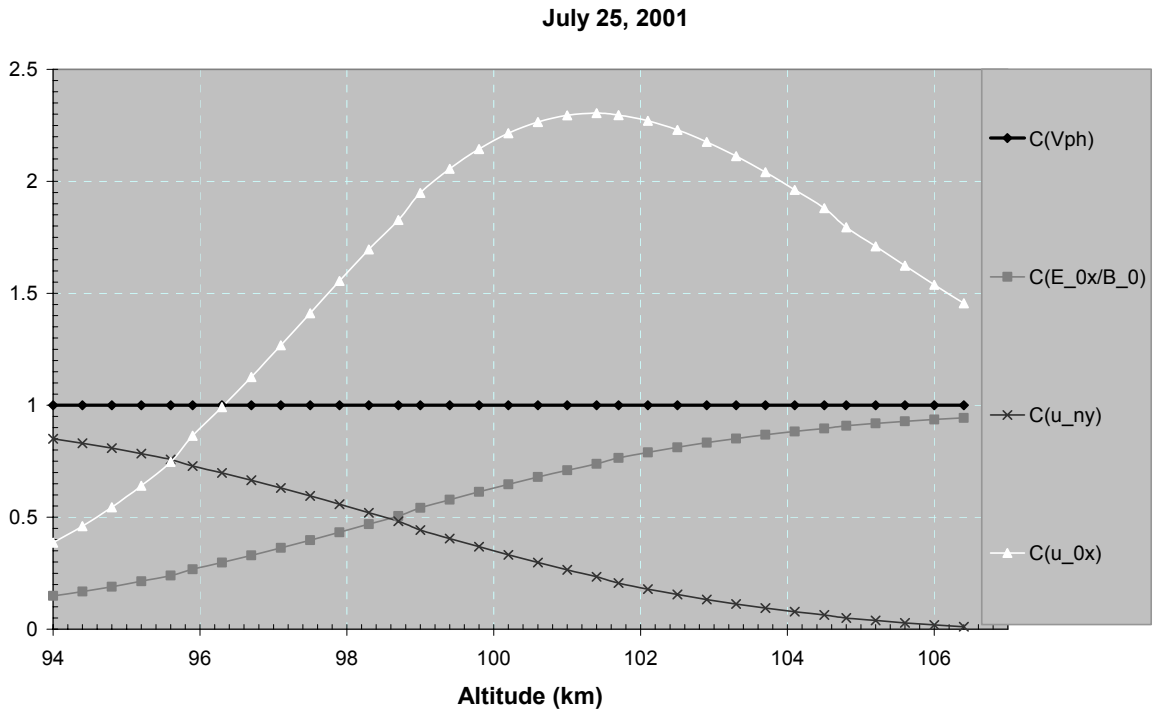
July 25, 2001
2.5
2
1.5
1
0.5
0
94
96
98
100
102
104
106
Altitude (km)
C(Vph)
C(E_0x/B_0)
C(u_ny)
C(u_0x)

Fig. 3a

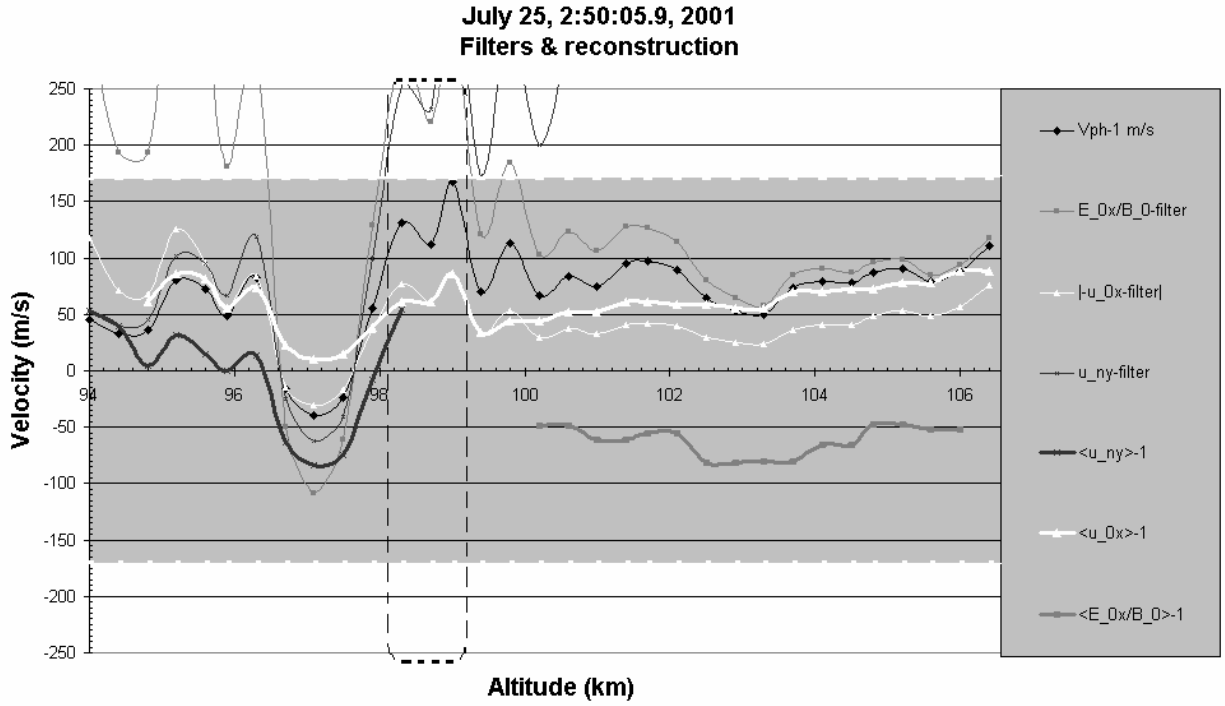
July 25, 2:50:05.9, 2001
Filters & reconstruction
Velocity (m/s)
250
200
150
100
50
0
-50
-100
-150
-200
-250
94
96
98
100
102
104
106
Altitude (km)
Vph-1 m/s
E_0x/B_0-filter
|-u_0x-filter|
u_ny-filter
<u_ny>-1
<u_0x>-1
<E_0x/B_0>-1

Fig. 3b

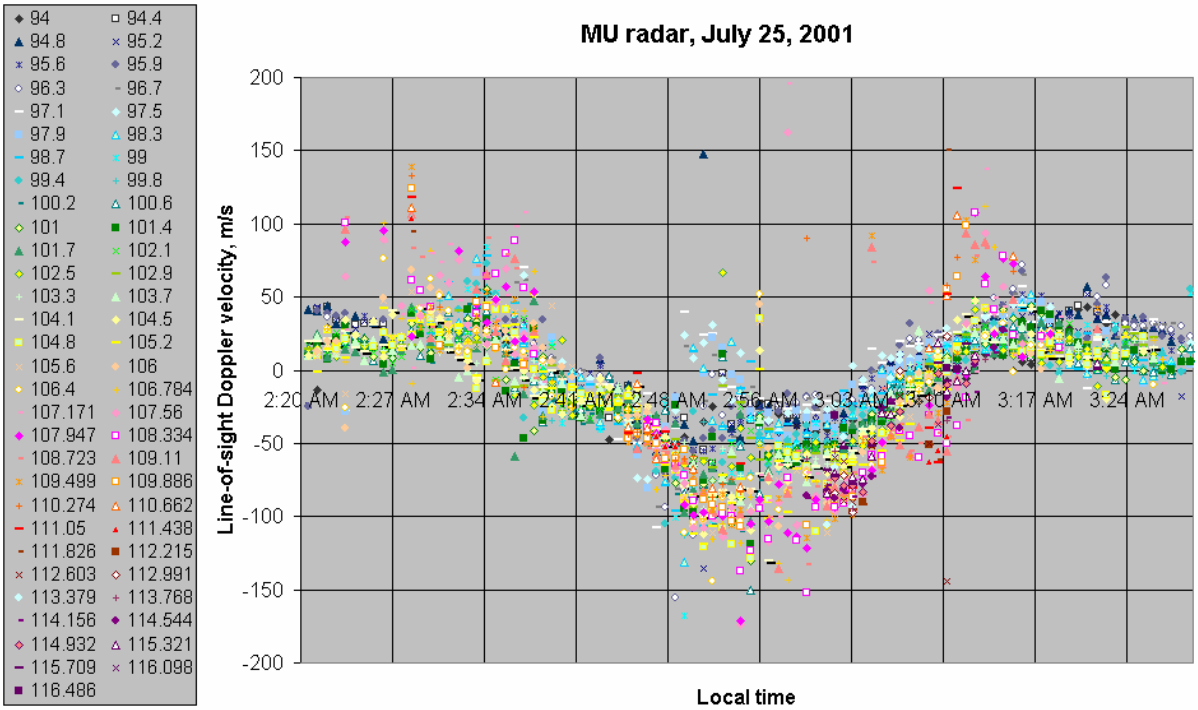
MU radar, July 25, 2001
Line-of-sight Doppler velocity, m/s
Local time
200
150
100
50
0
-50
-100
-150
-200
2:20 AM
2:27 AM
2:34 AM
2:41 AM
2:48 AM
2:56 AM
3:03 AM
3:10 AM
3:17 AM
3:24 AM
94
94.4
94.8
95.2
95.6
95.9
96.3
96.7
97.1
97.5
97.9
98.3
98.7
99
99.4
99.8
100.2
100.6
101
101.4
101.7
102.1
102.5
102.9
103.3
103.7
104.1
104.5
104.8
105.2
105.6
106
106.4
106.784
107.171
107.56
107.947
108.334
108.723
109.11
109.499
109.886
110.274
110.662
111.05
111.438
111.826
112.215
112.603
112.991
113.379
113.768
114.156
114.544
114.932
115.321
115.709
116.098
116.486

Fig. 4

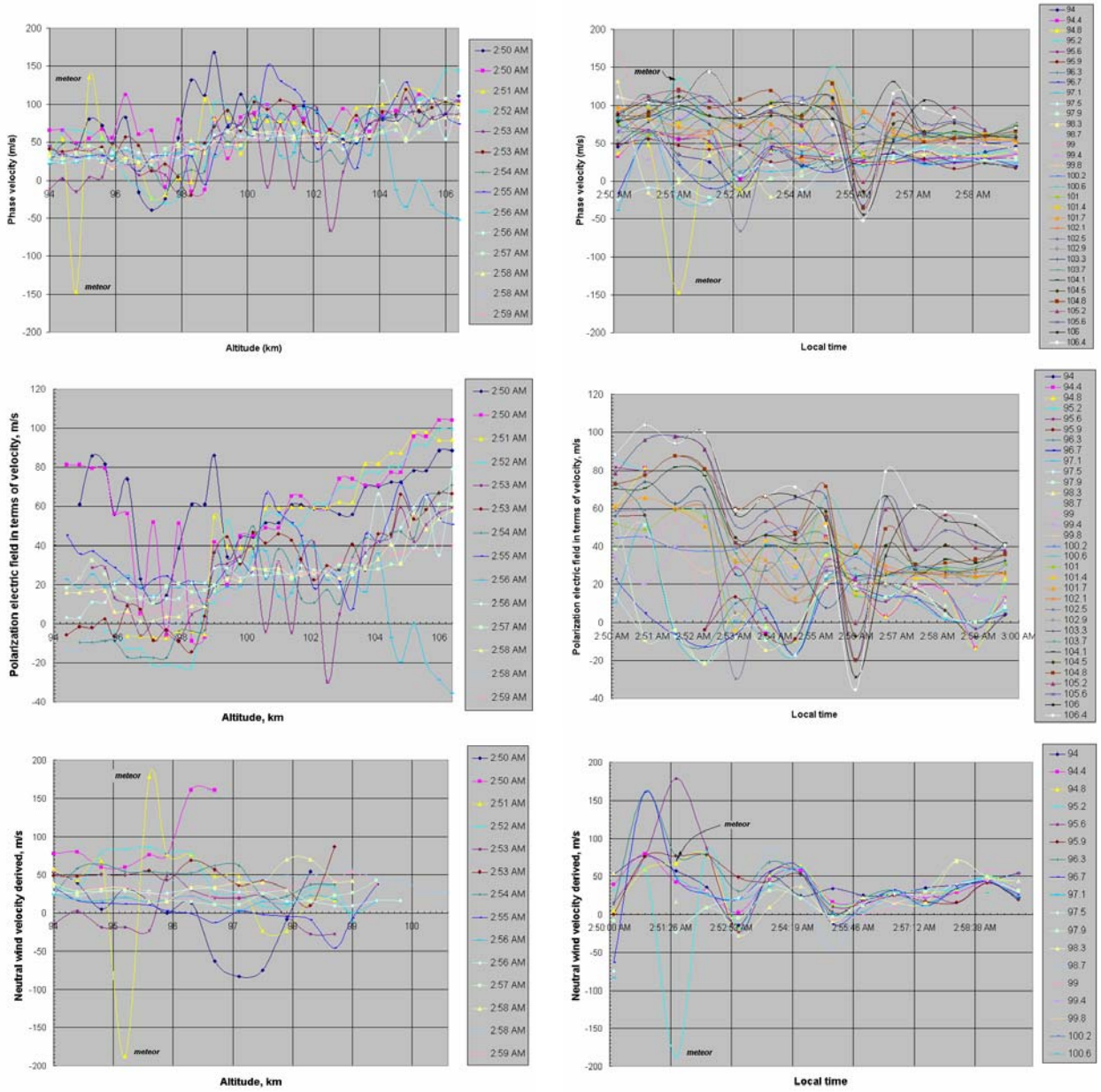
Phase velocity (m/s)
meteor
Altitude (km)
Local time
Polarization electric field in terms of velocity, m/s
Altitude, km
Local time
Neutral wind velocity derived, m/s
Altitude, km
Local time

Fig. 5